Two-Phase Flow Modelling of Metal Vaporisation under Static Laser Shot using a Double Domain ALE Method – A Feasibility Study

Y. A. Mayi*[1, 3], M. Dal[1], P. Peyre[1], M. Bellet[2], C. Metton[3], C. Moriconi[3], R. Fabbro[1]

1. PIMM Laboratory, UMR 8006 Arts et Métiers-CNRS-CNAM, 75013 Paris, France
2. CEMEF, UMR 7635 PSL Research University MINES ParisTech, 06904 Sophia Antipolis, France
3. Safran, 75724 Paris Cedex 15, France

* Corresponding author: yaasin.mayi@ensam.eu (Y. A. Mayi)

Abstract

As the Layer Beam Melting (LBM) technology – also referred to as Selective Laser Melting (SLM) – is garnering industrial interest, understanding of the associated physical phenomena is necessary to control the process. Particularly, metal vaporisation generates melt pool instabilities and collateral effects – powder bed denudation or ejection of melt and particles – which are the source of defects as inclusions, porosities and cracks. The present study is a first step toward the multiphase analysis of vaporization under laser irradiation. A 2D axisymmetric static laser shot model, without powder, is developed to compute and couple fluid flows and heat transfers in the melt pool and in the gas phase. The liquid/vapour interface is tracked with the Arbitrary Lagrangian Eulerian (ALE) method and relevant jump conditions are used to couple the two separated domains. Melt pool shape and dimensions as well as thermal and fluid flow are analysed and compared to experimental observations and analytical models.

Keywords: Laser drilling, Laser Beam Melting (LBM), Selective Laser Melting (SLM), Additive Manufacturing (AM), keyhole, vapour plume, melt pool, ejections, Arbitrary Lagrangian Eulerian (ALE).

I. Introduction

LBM is an Additive Manufacturing (AM) technology where successive layers of metal powders are selectively melted by a laser beam, following a computer-programmed pattern. The whole is performed in a building chamber filled with inert gas, argon typically. This process is garnering industrial attention as the shape flexibility it allows, gives the opportunity to rethink the components and their functionalities. Compared with Layer Metal Deposition (LMD) techniques, LBM allows higher geometrical resolution and lower roughness, due to the dimension of the melted zones – of the order of 100 µm for LBM and of the millimetre for LBM – but at the cost of a relatively poor building rate[1]. The application of LBM includes high added value components in the aerospace field, such as turbine distributor, or tailored implants for the medical sector.

Based on the interaction between a laser beam and a powder bed (Figure 1), the process is associated with complex physical phenomena which lead to defects as porosities or inclusions. Many experimental studies are dedicated to understanding those phenomena, which one may summarize as following. First, the powder bed absorbs the laser energy. Thus the powder grains melt, bond together, wet the substrate – or the previous melted layer – and form a melt pool. Some powder grains may partially or entirely attaint the alloy vaporisation temperature, creating vapour or grain ejections[2]. Then, thermocapillary convection stirs the melt because of strong temperature gradients (>10^6 K/m)[3]. Finally, if the melt pool surface reaches the alloy boiling temperature, then the generated recoil pressure deforms the melt pool[4], forming a "keyhole". This pressure becomes the main driving force of the melt[5]. At the same time, metal vapour is ejected at high speed – potentially at the local speed of sound[6] – and is reported to generate a recirculation flow which drags the powder particle to the melt pool or ejects them upward[2,4,7]. Consequently, a powder denudation zone around the melt track is created and the ejected heat-affected particles may contaminate the surrounding powder bed.

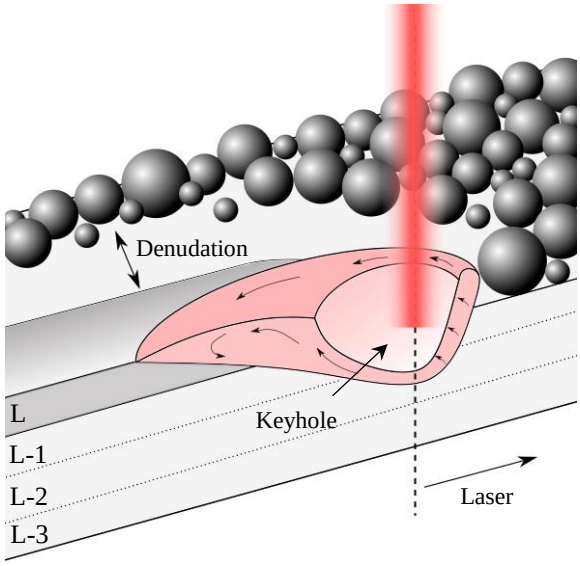

Figure 1 Principle of the SLM process.

In addition to experimental work, analytical and numerical models address the previous issues.

Gusarov and Smurov[8] developed an analytical model which predicts the equivalent laser heat source generated within the powder bed due to the multiple-reflexions of the laser irradiation, assuming a homogeneous absorbing scattering powder bed. This behaviour predicted by their model has been confirmed by numerical work performed by Dayal et al.[9] who used a ray tracing approach. However, if this in-depth energy absorption is valid for the very first steps of laser-matter interaction, then the laser mainly interacts with the melt[10].

Regarding the specific phenomenon of metal vaporisation under laser irradiation, analytical models have widely been used in the context of laser drilling and welding.

The so-called "piston model", developed by Semak and Matsunawa[11] studies the role of recoil pressure on the mass and energy balance of a cylindrical liquid cell, irradiated by a laser beam (Figure 2b). This simplified approach predicts for a given absorbed intensity, good orders of magnitude of the steady-state liquid surface temperature and of velocities characteristic to laser drilling. Similarly, Fabbro et al.[12] proposed a model which estimates the keyhole depth and inclination during laser welding. Regarding the gas side, several authors as Samokhin[13] or Knight[14] derived analytical models which estimate the order of magnitude of the steady-state metal vapour velocity magnitude. These approaches assume a local 1D flow and solve the energy and mass balance across the Knudsen layer (Figure 2c).

There are also an increasing number of numerical models which address the complex physics depicted previously. Khairallah et al.[15] proposed a multi-physical model, with the use of an in-house ALE algorithm, which solves the melt flow – including surface tension, thermocapillary convection and recoil pressure – and its interaction with the surrounding powder grains. Similarly, Tang et al.[16] studied the possible pore formation due to keyhole closure with a Volume of Fluid method. Also, Chen et al.[17] proposed an alternative Level-Set (LS) approach where the powder bed is modelled with an equivalent homogeneous absorbing medium. This approach allows saving computational resources but disregards the fine melt pool-powder grain interaction.

However, the models cited previously do not address the metal vapour flow. Bidare et al.[7] recently proposed a simplified numerical model to compute the induced gas flow but without addressing the melt flow. Previously, Courtois et al.[18] developed a two-phase flow LS model (with COMSOL Multiphysics®) of laser welding, but focused their analysis on the metal phase.

Consequently, the present work studies the feasibility toward coupling the melt and the vapour flow. The powder layer is first omitted and computation is performed on a 2D axisymmetric geometry (Figure 2a) to save numerical resources.

The paper firstly introduces the physical model, including the assumptions and the mathematical formulations. Then, the results are presented and discussed in the light of experimental and analytical considerations. Finally, a conclusion is made and future developments are described.

II. Numerical Model and Experimental Setup

A. The Double Domain ALE Model

The physical model is implemented in COMSOL Multiphysics® 5.3a. It solves transient heat law (1), mass (2) and momentum (3) conservation in both the metal and the gas domains.

$$\rho c_p^{eq}\frac{\partial T}{\partial t}+\rho c_p\left(\vec{u}\cdot\vec{\nabla}T\right)=\vec{\nabla}\cdot\left(k\vec{\nabla}T\right) \tag{1}$$

$$\frac{\partial \rho}{\partial t}+\vec{\nabla}\cdot(\rho\vec{u})=0 \tag{2}$$

$$\rho\frac{\partial \vec{u}}{\partial t}+\rho\left(\vec{u}\cdot\vec{\nabla}\right)\vec{u}=\vec{\nabla}\cdot\left\{-pI+\mu\left[\vec{\nabla}\vec{u}+\left(\vec{\nabla}\vec{u}\right)^T\right]-\frac{2}{3}\left(\vec{\nabla}\cdot\vec{u}\right)I\right\}+K\vec{u}+\rho\vec{g} \tag{3}$$

ρ [kg/m3]: density; c_p [J/kg/K]: specific heat; k [W/m/K]: thermal conductivity; μ [Pa.s]: dynamic viscosity

Notice that the liquid metal is assumed incompressible, hence, $-\frac{2}{3}\left(\vec{\nabla}\cdot\vec{u}\right)I$ vanishes and $\vec{\nabla}\cdot\vec{u}=0$. Latent heat of melting is integrated through an equivalent specific heat (4).

$$c_p^{eq}=c_p+\frac{L_m}{\sqrt{\pi\Delta T^2}}\exp\left[-\frac{(T-T_m)^2}{\Delta T^2}\right] \tag{4}$$

$T_m=\left(T_{liquidus}+T_{solidus}\right)/2$; *2ΔT: solidification interval*

Darcy's penalisation law models the solid/liquid transition in the metal phase (5).

$$K=C_1\frac{\left(1-f_{liq}\right)^2}{f_{liq}^3+C_2} \tag{5}$$

In the liquid (f_{liq} = 1), K = 0 and one finds the classical Navier-Stokes (NS) equations. Conversely in the solid (f_{liq} = 0), K → ∞, thus the velocity field tends toward zero.

The ideal gas phase is assumed (6).

$$\rho=\frac{p\widetilde{M}}{RT} \tag{6}$$

$\widetilde{M}$ [kg/mol] is the averaged molar mass (7) computed thanks to the Fick's law (8).

$$\widetilde{M}=\omega M_{metal}+(1-\omega)M_{argon} \tag{7}$$

$$\frac{\partial \omega}{\partial t}+\vec{\nabla}\cdot\left(-D\vec{\nabla}\omega\right)+\vec{u}\cdot\vec{\nabla}\omega=0 \tag{8}$$

D [m²/s]: diffusion coefficient

ω = 1 at the liquid/vapour interface.

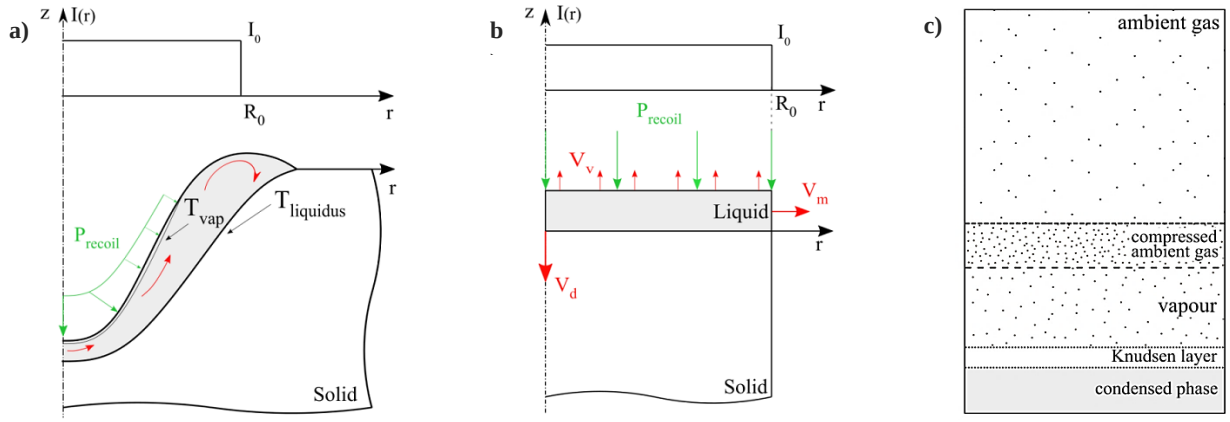

Figure 2 Schematics of **a)** Laser drilling keyhole. **b)** The piston model. **c)** 1D gas flow structure for the Knudsen approach.

1. Boundary Conditions

A homogeneous (top hat) laser heat flux is imposed on the metal/gas interface (9).

$$\varphi_{laser} = A(\theta)cos(\theta)\frac{P}{\pi R_0^2}g(t) \quad (9)$$

A: absorptance of the substrate; θ [rad]: angle of incidence; P [W]: laser power; R_0 [m]: laser spot radius; g(t): temporal profile of the laser pulse

The material absorptance is calculated thanks to the Fresnel laws[18]. Laser intensity is counterbalanced by vaporisation losses (10), conduction and convection within the metal phase. Radiation and external convection are neglected.

$$\varphi_{vap} = \dot{m}L_v \quad (10)$$

$\dot{m}$ [kg/m²/s]: vaporisation flux; L_v [J/kg]: latent heat of vaporisation

The mass vaporisation flux is calculated thanks to equation (11) derived by Samokhin[13].

$$\dot{m} = (1-\beta)\sqrt{\frac{M}{2\pi RT}}P_{sat}(T) \quad (11)$$

β: retro-diffusion coefficient; R [J/mol/K]: universal gas constant; P_{sat} [Pa]: saturated vapour pressure

β represents the fraction of evaporated particles which recondensates when they interact with the surrounding gas. At high evaporation rates such as encountered in SLM, β tends to its lower limit which is 0.17[13]. The saturated vapour pressure is calculated thanks to the Clausius-Clapeyron law (12).

$$P_{sat}(T) = P_{amb}exp\left[\frac{ML_v}{RT_V}\left(1-\frac{T_V}{T}\right)\right] \quad (12)$$

P_{amb} [Pa]: ambient pressure; T_V [K]: boiling temperature

Also, when the melt reaches the vaporisation temperature, a recoil pressure is applied on the liquid/gas interface (Figure 2). In case of high vaporisation rate, this is expressed thanks to Samokhin's model[13] (13)

$$P_{recoil} = \frac{1}{2}(1+\beta)P_{sat}(T) \quad (13)$$

One understands there are two contributions: from the evaporated particle because of the action-reaction principle $\left(\frac{1}{2}P_{sat}\right)$ and from the re-condensing ones $\left(\frac{1}{2}\beta P_{sat}\right)$. However this model is valid only at temperature much greater than the boiling temperature, when vaporisation is intense enough to expel the surrounding gas atoms (or in the vacuum). Pang et al.[19] generalised the previous law for the whole temperature range. For conciseness purpose, Pang's model is not detailed here. Please report the dedicated paper.

The model also integrates surface tension and thermocapillary convection (14).

$$\vec{f}_\sigma = \sigma\kappa\vec{n} + \vec{\nabla}_S\sigma \quad (14)$$

σ [N/m]: surface tension

Finally, regarding vapour generation, the key is simply the expression of the jump conditions. At the interface, the phases normal velocities are linked via their respective densities, the interface velocity and the vaporisation flux (15).

$$\rho_v(\vec{u_v}\cdot\vec{n} - V) = \rho_l(\vec{u_l}\cdot\vec{n} - V) = \dot{m} \quad (15)$$

V [m/s]: interface velocity

The density of the vapour phase is computed thanks to the ideal gas law, assuming the pressure to be the saturated vapour pressure. This means that the evaporating particles are supposed to be in thermodynamic equilibrium with the liquid, just before vaporisation[14].

2. Mesh Optimisation

ALE is an interface-tracking method which combines the advantage of the eulerian description (modelling high deformation) to that of the lagrangian description (fine resolution of the interface). The mesh vertices positions are first calculated in lagrangian and then,

according to an arbitrary smoothing method selected to minimise mesh distortion and to avoid elements entanglement, the vertices either stay fixed (eulerian), or moves with the fluid particles (lagrangian) or moves to an arbitrary prescribed position. It is thus necessary to limit mesh distortion at the laser/matter interaction zone, where a fine resolution is needed. To do that, mesh deformation is firstly managed with the "Yeoh smoothing"[20] method, which attributes to the mesh elements a stiffening factor (equals to 100 by default). When the mesh deforms, the distorted elements stiffen so that the distortion is better distributed to the entire mesh. The higher the stiffening factor, the lower is the individual element deformation. Secondly, the initial elements aspect ratio is shrunk along (O,z) in the gas domain – as they are expected to elongate during the drilling – and on the contrary, they are elongated in the metal phase.

3. About the Double Domain ALE Approach

In the double domain ALE approach, the two-phase flow problem is solved using a single ALE algorithm – which tracks the liquid/gas interface – but two sets of NS equations. Information from one fluid to the other are transferred via the jump conditions (15).

This approach offers a high modelling flexibility. First, it handles fluids with different characteristics. For example, an incompressible fluid (liquid metal) can be coupled with a compressible one (gas). In other two-phase flow methods – LS for instance – incompressibility hypothesis is usually formulated for the two fluids in an undifferentiated way. Also, our method gives the user some analysis choice. One may compute the metal phase only, if the vapour plume has limited impact on the melt pool. For instance, in the case of shallow or vertical keyholes, one may reasonably assume that the vapour plume do not shear the melt flow (decoupled). If the users are still interested in the gas flow, they may subsequently compute the gas phase (one-way coupling). Finally, if the vapour has an impact on the melt pool (inclined keyhole), the two-way coupled option is still feasible.

B. Experimental Setup

Laser drilling experiments are carried out using Inconel® 625 plates, on an instrumented setup equipped with a Yb:YAG laser operating at 1030 nm, a local argon shielding device and a rapid camera. These experiments aim to validate the simulated melt pool dimensions (width and depth). The experimental parameters are summarized in Table 1.

Table 1 Experimental parameters.

P [W]	D_0 [µm]	τ_{pulse} [ms]
320 - 500 - 700	205 (top hat)	3

Analysing drilled holes is rather difficult and time consuming with traditional techniques (radiography or longitudinal section) due to the expected holes dimensions. So to conduct this investigation, the so-called Direct Observation of Drilled hOles (DODO) method is implemented (Figure 3).

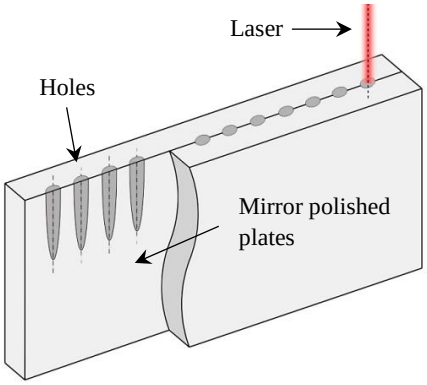

Figure 3 Schematic of the DODO method.

This method consists of drilling on the joint of two pre-polished plates in butt configuration[21]. This facilitates merging the drilling axis with the analysis plane – controlled with the rapid camera – and allows analysing tens of holes in the same procedure.

III. Results and Discussion

Material's thermo-physical properties are taken from Mills[22] and Lange's Handbook of Chemistry[23]. Simulations where run on a 16-cores station with 126 Gio RAM. CPU time for the full two-phase flow model was about four hours.

A. Heat Transfer in the Melt Pool

Considering the experimental configuration and the results (shallow vertical melted zones with an aspect ratio $R = \text{depth}/\text{width} < 0.5$), decoupled simulations have firstly been performed to compare the dimensions and the shape of the melted zones (Figure 4).

When compared with the experimental results (Figure 4, Figure 5), it appears that the Finite Element Model (FEM) provides good estimations of the melted zone morphology and dimensions. The melt pool width is estimated within 5% of the experimental mean value whereas the melt pool depth is overestimated by about 7%. Notice that considering the experimental dispersion (an average of ±4% for the width and ±13% for the depth, 15 holes per parameters), these estimations are very satisfying.

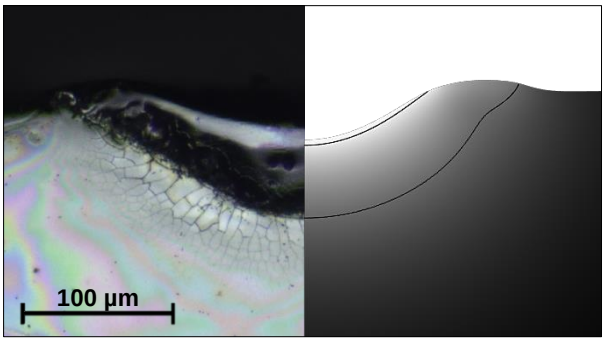

Figure 4 Comparison of melted zone given by experiment and FEM | P = 320 W, D_0 = 205 µm, τ_{pulse} = 3ms.

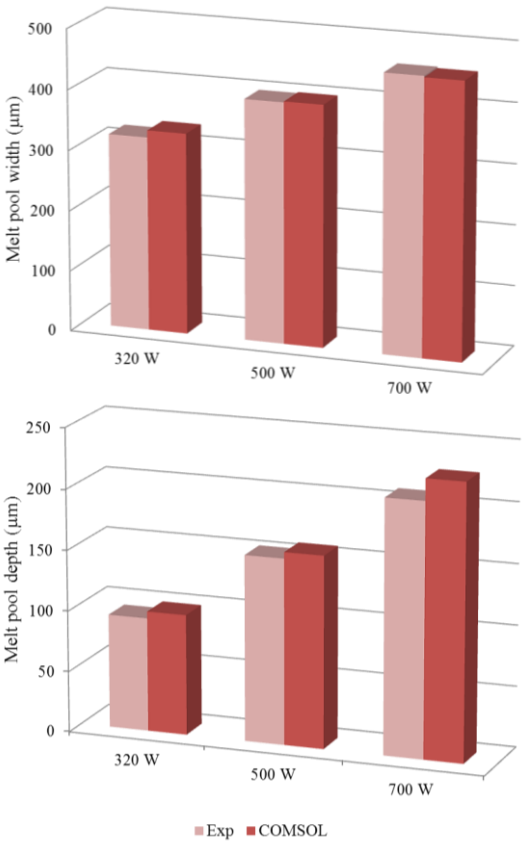

Figure 5 Comparison between simulated and experimental melt pool width and depth.

This agreement between experimental and numerical results is a first indication that the present FEM provides a good description of the melt pool thermo-hydraulics. Direct measurement of the melt pool temperature has not been conducted here, but in order to analyse and validate the global thermal field, our numerical model is compared to the reference analytical model of laser drilling: the piston model. Since Semak and Matsunawa[11], this model has been updated several times. We followed Hirano's recommendations[5].

Figure 6a compares the liquid surface temperatures estimated by the piston model and by our FEM. Figure 6b shows the absorbed laser power distribution between convection, conduction and vaporisation, as estimated by the piston model. These data are plotted against a range of absorbed intensity, corresponding to laser powers from 320 W to 700 W, on a 150 µm spot with a normal absorptance of 0.3. The piston model assumes a homogeneous surface temperature whereas in fact, the temperature reaches its maximum at the symmetry axis and decreases on the edge of the melt pool by convection. Thus, the analytical result is compared to the maximum and the average (on D_0) temperature obtained numerically.

The reader may first notice the similar temperature trends predicted by the two models. Especially, the numerically estimated maximum temperature is shifted by +9% compared to the piston estimation. The average temperature predicted by the FEM is on average 3% higher than that predicted by the piston model. However, the simulated average temperature does not increase as fast as the analytic one. This is not surprising, because the piston model assumes a horizontal melt pool surface during the whole process, hence a constant normal laser absorption (Figure 2). This is not the case in the FEM. Due to the keyhole curvature (Figure 2, Figure 4), the absorbed intensity is normal only at the melt pool centre and decreases with the angle of incidence (equation 9). Hence, the deeper the keyhole is (the higher the incident intensity is), the wider the (low absorbing) inclined melt pool surface within D_0. Consequently with our model, the average surface temperature does not grow as fast as the maximum temperature.

In reality, one must also take into account the multiple-reflexion in the keyhole which consequently increases the global laser power absorption.

Also, the vaporisation temperature at atmospheric pressure of Inconel® 625 is about 3200 K (Clausius-Clapeyron law). Here the study indicates that the melt pool surface exceeds this temperature due to the local pressure increase (because of the recoil pressure).

Finally, Figure 6b clearly highlights the major role played by melt convection in the power exchange. In the selected laser/matter regime, melt pool convection mainly driven by the recoil pressure is by far the dominant heat exchange mechanism – up to 70%. Hence, to correctly predict the vapour plume velocity which depends on the surface temperature (equation 14), it is of a major importance to accurately describe the melt-pool hydrodynamics.

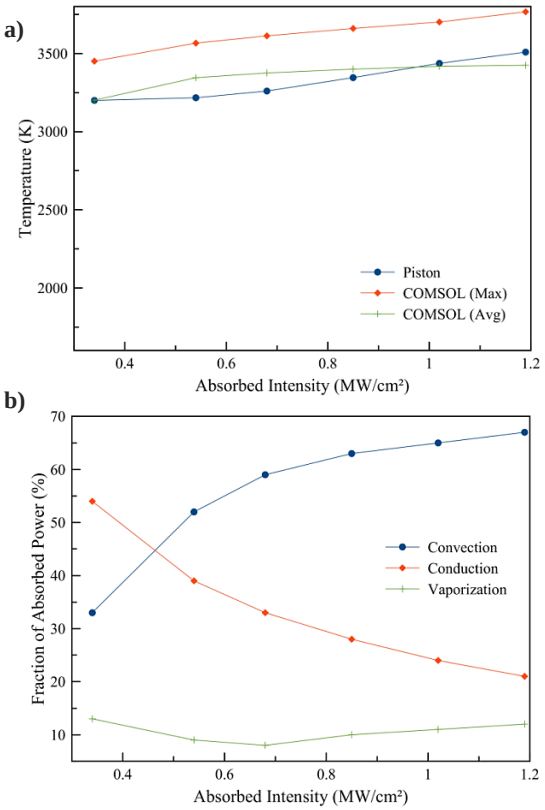

Figure 6 a) Surface temperature against absorbed laser intensity. **b)** Absorbed power distribution against absorbed laser intensity | D_0 = 150 µm, τ_{pulse} = 3 ms.

B. Vapour Flow

The following aspect is the real added-value of our work. A numerical model such as proposed here may be of a valuable help to understand the vaporisation-

induced collateral effect encountered in SLM. Direct visualisation of the metal vapour plume has not been conducted here. Thus, the structure of the simulated gas flow is qualitatively analysed in the light of the literature results, and the quantitative results are compared to Knight's analytical model. Notice that the following results have been simulated in two-way coupling mode, even if in 2D axisymmetric the vapour plume has a limited impact on the melt.

Figure 7 depicts the very first stage of vaporisation. On the left-hand side, the streamlines indicate that the vapour plume generates a recirculation flow on its side. This phenomenon is reported[2] to cause denudation. Notice that the plume velocity increases very quickly as the melt pool temperature exceeds rapidly the boiling point – more than 100 m/s after 4e-5 s and up to 450 m/s after 0.3 ms. On the right-hand side, the fraction of metal vapour contours highlights a mushroom structure characteristic of the Rayleigh-Taylor instability – a lighter fluid pushing on a denser fluid. This flow structure has been observed in SLM experiments[7].

Figure 8 compares the local Mach numbers – i.e. the Mach number at the vicinity of the liquid/vapour interface in the FEM (on the symmetry axis) and just outside of the Knudsen layer in Knight's model. As a reminder, the Mach number is defined as $\mathrm{Ma} = \mathrm{U}/c$, where U is the velocity magnitude, $c = \sqrt{\gamma p/\rho}$ is the local speed of sound and γ is the adiabatic index (equals to 5/3 for a monoatomic gas).

The two models predict similar order of magnitude of local Mach number – with an average relative difference of 15%. However, the trends are different. The FEM model first overestimates the local Mach number which then stagnates (or increases very slowly) whereas the local Mach number computed by Knight increases faster.

These differences might be explained by the choice of the vaporization flux expression. We have chosen the simplified Samokhin's law, as it is easier to implement (equation 11). This law assumes that the vaporisation flux depends only on the local temperature, with a constant retro-diffusion coefficient β. On the contrary, Knight's model is more coupled. The vaporisation flux depends on the melt temperature as well, but also on a function of the local Mach number[14] (16).

$$\dot{m} = \sqrt{\frac{\mathrm{M}}{2\pi \mathrm{RT}}}\left[\mathrm{P_{sat}(T)} + \beta\sqrt{\frac{T}{T_{KN}}}\mathrm{P_{sat}}(\mathrm{T}_{KN})f(Ma)\right] \qquad (16)$$

T_{KN} [K]: temperature just outside the Knudsen layer

In practice, we find that vaporization flux predicted by Samokhin is first higher than that estimated by Knight and then between 3500 K and 3600 K (in our case), Knight's vaporization flux increases faster (Figure 9). The reader may notice that here, this local Mach crossing occurs at an absorbed intensity between 0.5 MW/cm² and 0.6 MW/cm² which precisely corresponds to a temperature between 3500 K and 3600 K (Figure 6a).

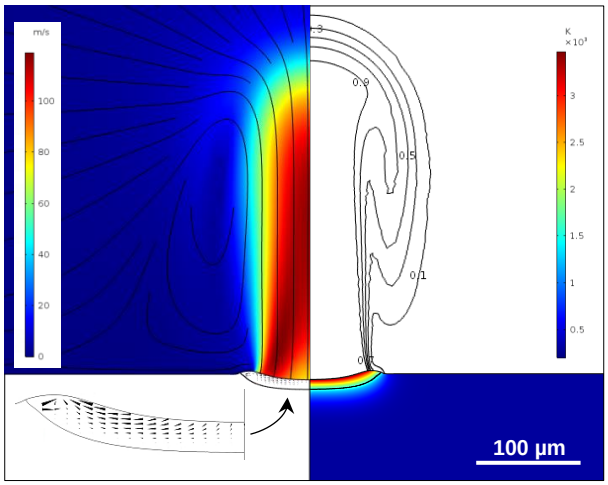

Figure 7 Melt pool shape, gas velocity field and streamlines (left), melt pool temperature field and fraction of metal vapour contours (right) | P = 400 W, D_0 = 150 µm, t = 4e-5 s.

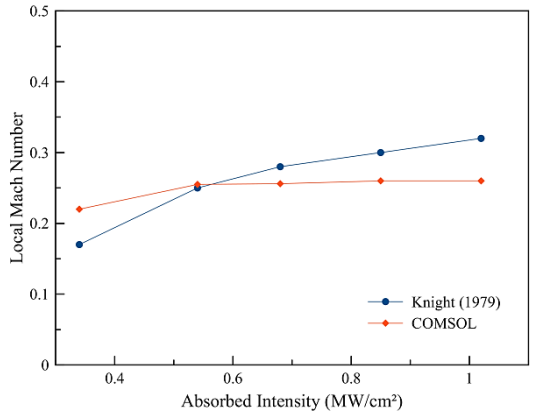

Figure 8 Local Mach number against absorbed laser intensity | D_0 = 150 µm, τ_{pulse} = 0.3 ms.

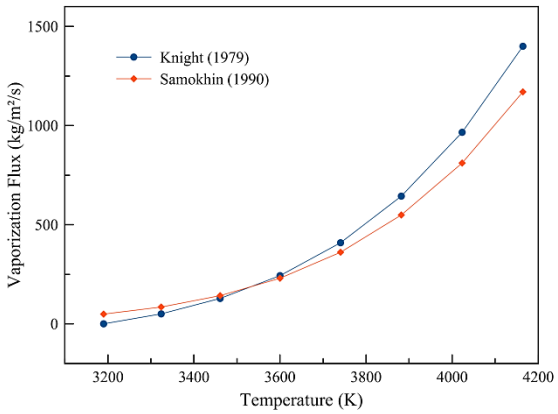

Figure 9 Comparison between the vaporization flux estimated by Knight and Samokhin.

IV. Conclusions and Outlook

We proposed a highly multi-physical model of metal vaporization under laser irradiation, which deals with compressible high-Mach number flow, heat transfer and transport of species. The proposed FEM has proven to be efficient to estimate the melt pool dimen-

sions in static configuration, which is the minimum requirement for such a model. The melt pool thermal behaviour and the vapour plume velocity have been validated with the help of analytical models. We have also reproduced some observed physical features such as the recirculation flow (partly responsible for the denudation phenomenon) and the occurrence of Rayleigh-Tailor instability, which gives the vapour plume its characteristic mushroom shape. Moreover, this approach provides modelling flexibility as the users may choose between modelling either the metal phase only, or the two phases in one-way or two-way coupling.

The main limitation of this FEM lies is the nature of the ALE method which, in principle, cannot handle topological change such as pore formation. This means that our model is limited to the low aspect ratio keyholes (< 2), when keyhole closure is less susceptible to occur. Regarding SLM and considering the usual industrial conditions, this does not limit the scope of our model. However, if one wants to apply this approach to, for instance, deep penetration welding, one must adapt the ALE method to handle topological changes.

Complementary work will have to be conducted. First, experimental validation should be extended to temperature measurement and to the evaluation of the vapour plume structure and velocity. Then, the model will have to be transposed to powder bed conditions, first in 2D axisymmetric and then in real 3D configuration.

V. References

1. Peyre, P., Dal, M., Pouzet, S. & Castelnau, O. Simplified numerical model for the laser metal deposition additive manufacturing process. *J. Laser Appl.* **29,** 022304 (2017).
2. Matthews, M. J. *et al.* Denudation of metal powder layers in laser powder bed fusion processes. *Acta Mater.* **114,** 33–42 (2016).
3. Debroy, T. *et al.* Additive manufacturing of metallic components – process, structure and properties. *Prog. Mater. Sci.* **92,** 112–224 (2017).
4. Gunenthiram, V. *et al.* Experimental analysis of spatter generation and melt-pool behavior during the powder bed laser beam melting process. *J. Mater. Process. Technol.* **251,** 376–386 (2017).
5. Hirano, K. Study on striation generation process during laser cutting of steel. (ENSAM, 2012).
6. Klassen, A., Scharowsky, T. & Körner, C. Evaporation model for beam based additive manufacturing using free surface lattice Boltzmann methods. *J. Phys. D. Appl. Phys.* **47,** (2014).
7. Bidare, P., Bitharas, I., Ward, R. M., Attallah, M. M. & Moore, A. J. Fluid and particle dynamics in laser powder bed fusion. *Acta Mater.* **142,** 107–120 (2017).
8. Gusarov, A. V. & Smurov, I. Radiation transfer in metallic powder beds used in laser processing. *J. Quant. Spectrosc. Radiat. Transf.* **111,** 2517–2527 (2010).
9. Dayal, R. & Gambaryan-Roisman, T. Heat transfer in granular medium for application to selective laser melting: A numerical study. *Int. J. Therm. Sci.* **113,** 38–50 (2017).
10. Teng, C., Ashby, K., Phan, N., Pal, D. & Stucker, B. The effects of material property assumptions on predicted meltpool shape for laser powder bed fusion based additive manufacturing. *Meas. Sci. Technol.* **27,** 085602 (2016).
11. Semak, V. & Matsunawa, A. The role of recoil pressure in energy balance during laser materials processing. *J. Phys. D. Appl. Phys.* **30,** 2541–2552 (1997).
12. Fabbro, R. *et al.* Analysis and possible estimation of keyhole depths evolution, using laser operating parameters and material properties. *J. Laser Appl.* **30,** 032410 (2018).
13. Samokhin. *Effect of Laser Radiation on Absorbing Condensed Matter*. *Proceedings of the Institute of General Physics* (1990).
14. Knight, C. J. Theoretical Modeling of Rapid Surface Vaporization with Back Pressure. *AIAA J.* **17,** 519–523 (1979).
15. Khairallah, S. A., Anderson, A. T., Rubenchik, A. & King, W. E. Laser powder-bed fusion additive manufacturing: Physics of complex melt flow and formation mechanisms of pores, spatter, and denudation zones. *Acta Mater.* **108,** 36–45 (2016).
16. Tang, C., Tan, J. L. & Wong, C. H. A numerical investigation on the physical mechanisms of single track defects in selective laser melting. *Int. J. Heat Mass Transf.* **126,** 957–968 (2018).
17. Chen, Q., Guillemot, G., Gandin, C.-A. & Bellet, M. Three-dimensional finite element thermomechanical modeling of additive manufacturing by selective laser melting for ceramic materials. *Addit. Manuf.* **16,** 124–137 (2017).
18. Courtois, M., Carin, M., Le Masson, P., Gaied, S. & Balabane, M. A complete model of keyhole and melt pool dynamics to analyze instabilities and collapse during laser welding. *J. Laser Appl.* **26,** 042001 (2014).
19. Pang, S., Hirano, K., Fabbro, R. & Jiang, T. Explanation of penetration depth variation during laser welding under variable ambient pressure. *J. Laser Appl.* **27,** 022007 (2015).
20. COMSOL Multiphysics®. User's Guide.
21. Schneider, M., Berthe, L., Muller, M. & Fabbro, R. A fast method for morphological analysis of laser drilling holes. *J. Laser Appl.* **22,** 127–131 (2010).
22. Mills, K. C. *Recommended values of thermophysical properties for selected commercial alloys*. *Journal of Chemical Information and Modeling* (Woodhead Publishing Limited, 2002).
23. Dean, J. A. *Lange's Handbook of chemistry*. (McGraw-Hill, 1972).

VI. Acknowledgements

The authors are grateful to Matthieu Schneider for his guidance on the DODO method, to Frédéric Coste, Socona Traoré and Thibault De Terris for their help with the experimental facilities and to Claude Verliac for his support in the sample preparation.